

Automated design of nonreciprocal thermal emitters via Bayesian optimization

Bach Do,^{*,†} Sina J. Ghalekohneh,[‡] Taiwo Adebisi,[†] Bo Zhao,^{*,‡} and Ruda Zhang^{*,†}

[†]*Department of Civil and Environmental Engineering, University of Houston, Houston, TX 77204, USA*

[‡]*Department of Mechanical Engineering, University of Houston, Houston, TX 77204, USA*

E-mail: bdo3@uh.edu; bzhao8@uh.edu; rudaz@uh.edu

Abstract

Breaking Kirchhoff’s law of thermal radiation has promised exciting new mechanisms for radiative heat rectification. However, an effective computational method to identify an optimal broadband nonreciprocal effect is still lacking. In this study, we present an optimization approach that achieves optimal broadband nonreciprocal effects in the infrared range of thermal radiation using doped magneto-optic InAs and Weyl semimetal materials. The optimization randomly starts with a less effective structure and incrementally improves the broadband nonreciprocity through the combination of reparameterization and Bayesian optimization. Optimization results show that the proposed approach can provide an optimal structure with fewer layers surpassing the performance of a current state-of-the-art design. Furthermore, the broadband nonreciprocal effect considerably increases when using InAs layers atop Weyl semimetal layers.

Keywords: Nonreciprocity, Thermal emitters, Gaussian process, Bayesian optimization, Reparameterization

Introduction

Over the past two decades, the control of thermal radiation transfer has gained significant interest due to its vital applications in spacecraft, manufacturing, thermal management, and energy conversion [1-4]. In most practical systems, thermal radiation exchange occurs through far-field electromagnetic waves between large-scale macroscopic surfaces. The design and simulation of these systems typically assume reciprocity in the transport process. For thermal emitters, the role of reciprocity is described by Kirchhoff's law [5,6] which states that the emissivity (ε) and absorptivity (α) are equal for a given direction, frequency, and polarization.

However, recent research advances [7-9] have suggested that reciprocity is not a requirement of thermodynamics, and it breaks down for nonreciprocal thermal emitters which allow ε and α to be separately controlled. Such unique systems promise an exciting new mechanism for radiative heat rectification that is required in record-breaking high-efficiency radiative energy harvesting [10-15], thermal regulation systems [16-19], and mechanical proportion with radiative heat flow [20,21]. Unlike near-field radiation exchange [22,23], effective far-field radiation transport relies on a broadband effect in the infrared range to carry energy. However, a mechanism that can provide optimal broadband nonreciprocal effect in the thermal infrared range is still lacking.

In this study, we optimize the nonreciprocal behavior of multi-layer structures using Bayesian optimization. Our approach focuses on enhancing broadband thermal emitters while considering both the magnitude of the contrast and the sign of the contrast between absorptivity and emissivity which designates the direction of the photon transport [21-2]. Additionally, this approach reduces the computational cost associated with calculating absorptivity and emissivity required for optimization. The structure studied here consists of two nonreciprocal materials: InAs, which requires an external magnetic field to exhibit nonreciprocity in the far-infrared, and Weyl semimetals, which show nonreciprocity without an external magnetic field in the mid-infrared and far-infrared ranges.

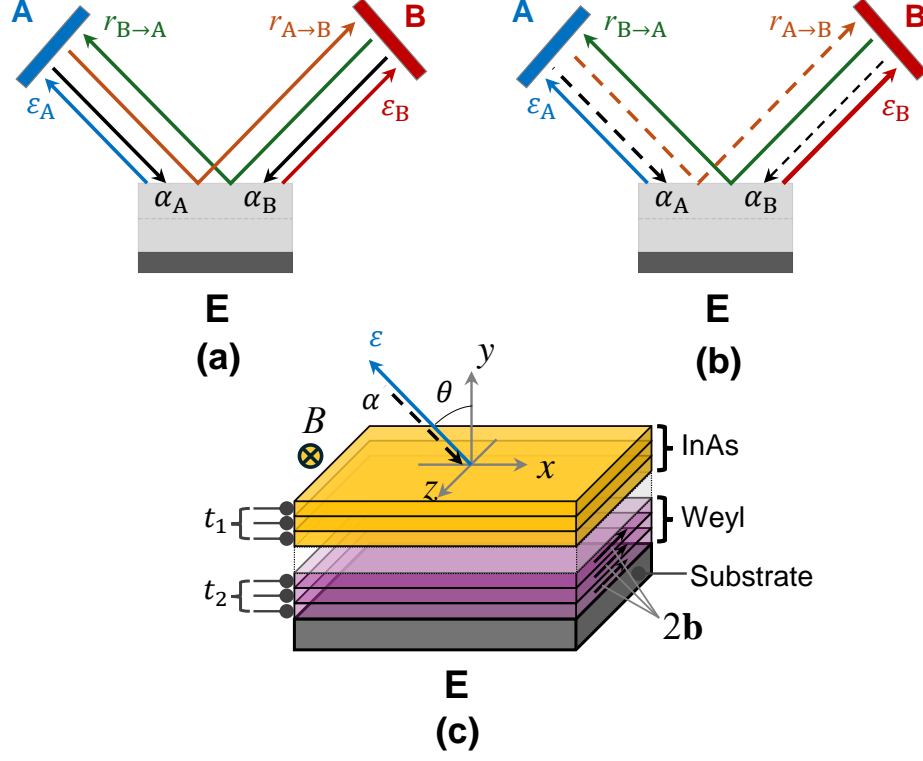


Figure 1: Illustration of radiative heat exchange between two blackbodies (A and B) and (a) a reciprocal emitter, and (b) a nonreciprocal emitter under thermal equilibrium. (c) Illustration of a multilayer structure consisting of InAs layers on top of Weyl semimetal layers on a reflective substrate.

Absorptivity and emissivity of nonreciprocal emitters

We introduce the method used to compute the absorptivity and emissivity of nonreciprocal emitters. Consider the system comprises an opaque thermal emitter (E) and two blackbodies, A and B, all at thermal equilibrium (Fig. 1(a)). According to the second law of thermodynamics, a portion of the emission from blackbody A is absorbed by the thermal emitter E (α_A), while the remaining part is reflected and subsequently absorbed by blackbody B ($r_{A \rightarrow B}$), leading to the following relationship:

$$\alpha_A + r_{A \rightarrow B} = 1, \quad (1)$$

where α_A represents the absorptivity in direction A at a specific wavelength, and $r_{A \rightarrow B}$ is the reflectivity from A to B at that wavelength.

Likewise, by considering emission from blackbody B, we have

$$\alpha_B + r_{B \rightarrow A} = 1. \quad (2)$$

Moreover, each blackbody absorbs and emits an equal amount of energy at thermal equilibrium, resulting in

$$\begin{aligned} \varepsilon_A + r_{B \rightarrow A} &= 1, \\ \varepsilon_B + r_{A \rightarrow B} &= 1. \end{aligned} \quad (3)$$

Combining Eqs. (1) to (3), we have

$$\alpha_A - \varepsilon_A = r_{B \rightarrow A} - r_{A \rightarrow B} = \varepsilon_B - \alpha_B. \quad (4)$$

For reciprocal emitters (Fig. 1(a)) where $r_{A \rightarrow B} = r_{B \rightarrow A}$, it follows that $\alpha_A = \varepsilon_A$ and $\alpha_B = \varepsilon_B$, which is consistent with Kirchhoff's law of radiation. However, for nonreciprocal emitters (Fig. 1(b)), we have $\alpha_A \neq \varepsilon_A$ and $\alpha_B \neq \varepsilon_B$ as $r_{A \rightarrow B} \neq r_{B \rightarrow A}$, which violates Kirchhoff's law of radiation. In this case, the absorptivity and emissivity of nonreciprocal emitters are derived from Eqs. (1) and (3), as

$$\begin{aligned} \alpha_A &= 1 - r_{A \rightarrow B}, \\ \varepsilon_A &= 1 - r_{B \rightarrow A}. \end{aligned} \quad (5)$$

In the exemplary structure shown in Fig. 1(c), we use InAs layers on top of Weyl semimetal layers on a reflective substrate. For the InAs layer, the magneto-optical (MO) response is utilized to break reciprocity. For transverse magnetic (TM) polarization with an electric field in the x - y plane, an external magnetic field B is applied along the z direction, following the Voigt geometry [24,25]. In the presence of B field, the permittivity tensor of

51 InAs reads [26]

$$\epsilon_{\text{InAs}} = \begin{bmatrix} \epsilon & i\eta & 0 \\ -i\eta & \epsilon & 0 \\ 0 & 0 & \epsilon_z \end{bmatrix}, \quad (6)$$

52 where the contrast $\eta(B\mathbf{z}) \neq 0$ represents how the permittivity changes in the presence of B
 53 compared with the absence of B . As we focus on epsilon-near-zero (ENZ) point where the
 54 material exhibits significantly enhanced MO strength [26-30] due to the diagonal elements of
 55 ϵ_{InAs} crossing zero at a specific frequency, the Voigt parameter $\varsigma = \eta(B\mathbf{z})/\text{Re}(\epsilon)$ approaches
 56 ∞ , and therefore, we observe a strong nonreciprocal effect.

57 The nonreciprocal effect is intrinsic for the Weyl semimetal layer and does not require
 58 an external magnetic field. The momentum separation of the Weyl cones, $2\mathbf{b}$, acts similarly
 59 to an applied magnetic field in magneto-optical systems. Consider the dielectric function of
 60 magnetic Weyl semimetals for TM polarization with an electric field in the x - y plane, where
 61 \mathbf{b} is oriented along the z direction, see Fig. 1(c). The dielectric tensor reads

$$\epsilon_{\text{Weyl}} = \begin{bmatrix} \epsilon_d & i\epsilon_a & 0 \\ -i\epsilon_a & \epsilon_d & 0 \\ 0 & 0 & \epsilon_d \end{bmatrix}. \quad (7)$$

62 Similar to InAs, the nonreciprocal effect for Weyl is significantly enhanced when the diagonal
 63 element ϵ_d crosses zero at ENZ point.

64 The ENZ point for the InAs and Weyl semimetal can be controlled by adjusting the
 65 carrier concentration and Fermi level, respectively. To achieve a broadband nonreciprocal
 66 effect, a multilayer structure of these materials can be utilized, with each layer having a
 67 different ENZ point. This results in nonreciprocal behavior over a broad wavelength range
 68 [32].

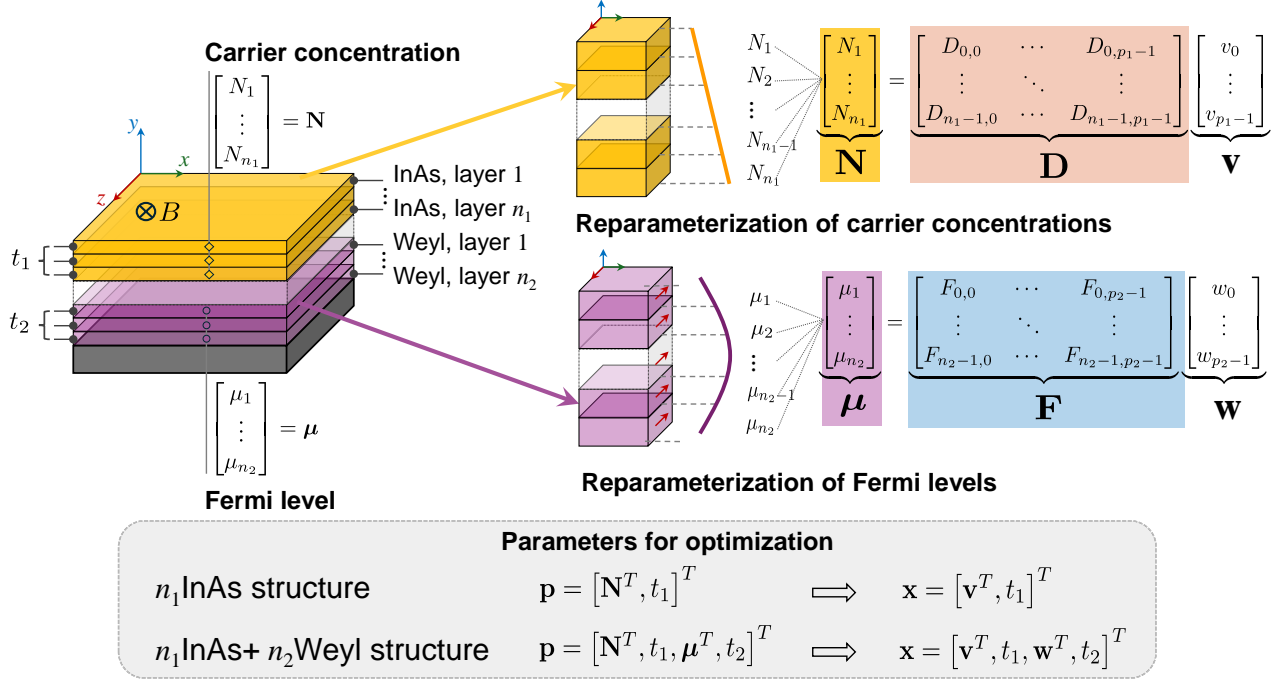


Figure 2: Design parameters \mathbf{p} for nonreciprocal emitters of interest, an example of the reparameterization strategy, and parameters \mathbf{x} for the optimization problem formulated after reparameterization. For a structure of n_1 InAs layers with distinct carrier concentrations and thickness t_1 , there are $n_1 + 1$ design parameters \mathbf{p} . For a structure of n_1 InAs layers with distinct carrier concentrations and thickness t_1 and n_2 Weyl semimetal layers with distinct Fermi levels and thickness t_2 , the number of design parameters \mathbf{p} is $n_1 + n_2 + 2$. After reparameterizing the carrier concentrations and Fermi levels, the numbers of optimization parameters for these structures are $p_1 + 1$ and $p_1 + p_2 + 2$, respectively, where p_1 and p_2 are the numbers of columns of \mathbf{D} and \mathbf{F} .

Optimization problem

To maximize the broadband nonreciprocity of a nonreciprocal thermal emitter of interest, we optimize the contrast between its absorptivity and emissivity. This involves determining an optimal set of the carrier concentration of InAs, the Fermi level of the Weyl semimetal, and the thickness of each layer in the structure. We let $\mathbf{p} \in \mathbb{R}_+^p$, $\lambda \in \mathbb{R}_+$, and $\theta \in \mathbb{R}_+$ represent the vector of design parameters for the nonreciprocal emitter, a value of wavelength, and a value of angle of incidence, respectively. We denote by $\alpha(\mathbf{p}, \lambda, \theta)$, $\varepsilon(\mathbf{p}, \lambda, \theta)$, and $\eta(\mathbf{p}, \lambda, \theta) = \alpha(\mathbf{p}, \lambda, \theta) - \varepsilon(\mathbf{p}, \lambda, \theta)$ the local functions for the absorptivity, emissivity, and contrast of this emitter, respectively.

Figure 2 shows the design parameters \mathbf{p} for a nonreciprocal thermal emitter, either composed of doped InAs layers or the combination of doped InAs layers on top of Weyl semimetal layers. For the structure of n_1 InAs layers, each with the same thickness, the design parameter vector \mathbf{p} consists of n_1 distinct carrier concentrations N_i ($i = 1, \dots, n_1$) and the thickness t_1 of each layer. For the structure of n_1 InAs layers at the top and n_2 Weyl layers at the bottom, \mathbf{p} includes n_1 distinct carrier concentrations N_i ($i = 1, \dots, n_1$) for the InAs layers, the thickness t_1 of each InAs layer, n_2 distinct Fermi levels μ_j ($j = 1, \dots, n_2$) for the Weyl semimetal layers, and the thickness t_2 of each Weyl semimetal layer.

We then formulate the following optimization problem for the nonreciprocal emitter:

$$\underset{\mathbf{p} \in \mathcal{P}}{\text{minimize}} \quad \tilde{\eta}(\mathbf{p}), \quad (8)$$

where $\tilde{\eta}$ represents the normalized contrast, which serves as the figure of merit for the broadband nonreciprocity of the emitter, and $\mathcal{P} \subset \mathbb{R}_+^p$ is the feasible domain of \mathbf{p} . The normalized contrast $\tilde{\eta}$ is defined as follows:

$$\tilde{\eta}(\mathbf{p}) = \frac{\int_{\lambda_L}^{\lambda_U} \int_0^{\pi/2} \eta(\mathbf{p}, \lambda, \theta) \sin \theta \cos \theta d\theta d\lambda}{\int_{\lambda_L}^{\lambda_U} d\lambda \int_0^{\pi/2} \sin \theta \cos \theta d\theta}, \quad (9)$$

where λ_L and λ_U are the lower and upper values of the considered wavelength range, respectively. The quadrature method for computing the numerator of $\tilde{\eta}(\mathbf{p})$ is given in the Supporting Information.

We further apply a reparameterization strategy to the objective function $\tilde{\eta}(\mathbf{p})$ to enforce desired design constraints on the emitter structure and/or other constraints on the optimization problem. The design constraints may include, for example, the distributions of carrier concentrations and Fermi levels over the material layers, while the optimization constraints ensure that the number of optimization parameters remains manageable for the optimizer, which is crucial when the number of design parameters \mathbf{p} is large, such as in cases with a large number of layers. Specifically, we transform $\tilde{\eta}(\mathbf{p})$ over the parameter space $\mathbf{p} \in \mathcal{P}$ into

$\bar{\eta}(\mathbf{x})$ over the space of optimization parameters $\mathbf{x} = \phi(\mathbf{p}) \in \mathbb{R}^d$, where the reparameterization map $\phi : \mathbb{R}_+^p \mapsto \mathbb{R}^d$ encapsulates all desired constraints. By optimizing $\bar{\eta}(\mathbf{x})$, we can leverage the encoded constraints to guide the optimization process with greater control. The optimization problem after reparameterization reads

$$\underset{\mathbf{x} \in \mathcal{X}}{\text{minimize}} \quad \bar{\eta}(\mathbf{x}), \quad (10)$$

where $\mathcal{X} = \{\mathbf{x} \in \mathbb{R}^d | \phi^{-1}(\mathbf{x}) \in \mathcal{P}\}$ with $\phi^{-1}(\mathbf{x}) = \mathbf{p}$. Thus, instead of solving problem (8) directly, we solve problem (10) and recover the optimal set of \mathbf{p} from the resulting optimal set of \mathbf{x} .

Given a specific value of the optimization parameters \mathbf{x} and the reparameterization map ϕ , computing $\bar{\eta}(\mathbf{x})$ is straightforward. We first compute the design parameter $\mathbf{p} = \phi^{-1}(\mathbf{x})$ associated with \mathbf{x} . We then compute $\tilde{\eta}(\mathbf{p})$ and set $\bar{\eta}(\mathbf{x})$ as $\tilde{\eta}(\mathbf{p})$.

Figure 2 illustrates the reparameterization technique used in this study. Specifically, we transform the carrier concentrations \mathbf{N} of the InAs layers and Fermi levels $\boldsymbol{\mu}$ of the Weyl semimetal layers into optimization parameters \mathbf{v} and \mathbf{w} , respectively, using two linear maps \mathbf{D} and \mathbf{F} . This transformation allows us to impose specific geometrical properties on the emitter, for example, linear profiles of carrier concentrations or quadratic profiles of Fermi levels (Fig. 2). By carefully designing the span of \mathbf{D} and \mathbf{F} , we can further control the number of the optimization parameters \mathbf{v} and \mathbf{w} , which significantly influences the efficiency and success of the algorithm chosen to solve the formulated optimization problem. We detail the method to compute \mathbf{D} and \mathbf{F} in the Supporting Information.

Optimizer

We use Bayesian optimization (BO)^{1,2} to solve problem (10) due to the high computational cost presented by the repeated calculation of the normalized contrast $\bar{\eta}(\mathbf{x})$ during optimization and the absence of gradient information for this objective function. This section provides

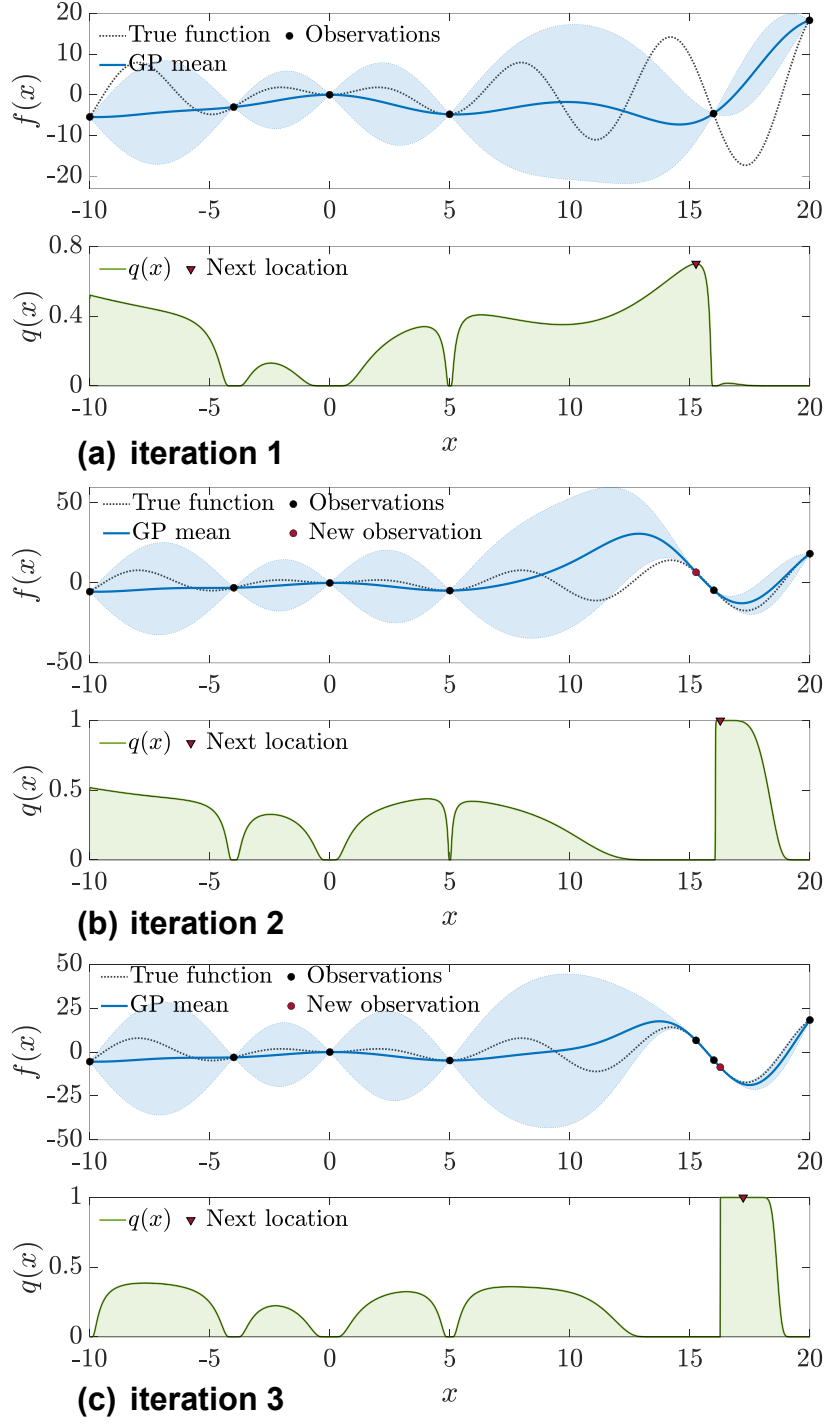


Figure 3: Schematic illustration of three consecutive iterations of BO for optimizing a univariate function $f(x)$. In each iteration, BO constructs a GP model for the objective function $f(x)$, formulates an acquisition function $q(x)$ based on the constructed GP model, and maximizes $q(x)$ for finding a new observation location that updates the GP model in the next optimization iteration.

an overview of BO and details how we leverage it to incrementally improve the broadband nonreciprocity of nonreciprocal emitters.

BO relies on two primary ingredients: a probabilistic model, which captures our prior knowledge about the objective function, and an acquisition function, which is an optimization policy to guide the optimization process. A Gaussian process (GP)³ model often serves as the probabilistic model due to its tractability and flexibility. Typically, the GP prior is specified simply by a zero mean function and a covariance function with a closed form and a few hyperparameters. Given a dataset of the objective function observations in each iteration of BO, the GP posterior can be derived by conditioning the prior model on the dataset using Bayes' theorem. This GP posterior then serves as the probabilistic model that approximates the costly objective function. The reader is referred to the Supporting Information for the mathematical foundation of GP and the analytical formula of the GP posterior.

It is worth noting that the dataset in each iteration of BO can include both numerical and experimental observations of the objective function. This allows for the integration of physical and mathematical understanding of the objective function into the optimization process.

Once the GP posterior model has been constructed, we formulate an acquisition function to define an optimization policy representing what we value in the current dataset. This acquisition function maps one of our preferences, including an improvement in the objective function value,^{4,5} a gain in information on the true minimizer,^{6,7} and a gain in information on the true minimum value,⁸ for the next design point to each point in the design variable space, considering our imperfect knowledge of the objective function. The formulated acquisition function is then numerically maximized using, for example, a global optimization algorithm to identify a new solution point that is used in the next iteration of BO. Maximizing the acquisition function is typically simpler and less computationally expensive than optimizing the costly objective function directly.

To this end, BO solves an optimization problem with a costly objective function by

repeatedly constructing a GP model for the objective function, formulating an acquisition function based on the constructed GP model, and maximizing the formulated acquisition function. This iterative process typically terminates as it reaches a prespecified number of observations of the costly objective function, which reflects our computational budget. Figure 3 illustrates three consecutive iterations of BO for minimizing a univariate objective function $f(x)$. BO starts with six observations of $f(x)$ and locates the true global minimizer of $f(x)$ after three iterations.

Algorithm 1 outlines the use of BO for optimizing a nonreciprocal thermal emitter of interest. We begin with specifying the design parameter domain \mathcal{P} , the number N of initial observations for evaluating the normalized contrast $\bar{\eta}(\mathbf{x})$, and the threshold K for the number of BO iterations, followed by defining the reparameterization map $\phi(\cdot)$ (Line 1). To construct an initial dataset \mathcal{D}_0 (Line 6), which is necessary for initializing BO, we randomly generate a set of N samples for the optimization parameters \mathbf{x} (Line 2), and subsequently evaluate $\bar{\eta}(\mathbf{x})$ at the generated samples using rigorous coupled-wave analyses (RCWAs) (Line 4). Here, we assume that the evaluated values of $\bar{\eta}(\mathbf{x})$ are noiseless, which means the numerical results perfectly capture the distribution of nonreciprocal thermal radiation in the emitter without introducing any numerical errors.

The main loop of BO (Line 8 to Line 16) starts by the construction of a GP posterior $\hat{\eta}_k(\mathbf{x})$ for $\bar{\eta}(\mathbf{x})$ from the current dataset \mathcal{D}_{k-1} (Line 10), where $k = 1, \dots, K$ represents the index variable for the loop. It then formulates an acquisition function $q(\mathbf{x})$ based on $\hat{\eta}_k(\mathbf{x})$ (Line 11) and maximizes $q(\mathbf{x})$ for a new observation \mathbf{x}_k of the optimization parameters (Line 12). To avoid reselecting points already in the current dataset \mathcal{D}_{k-1} , the constraint $\mathbf{x} \notin \mathcal{D}_{k-1}$ is imposed to the maximization of $q(\mathbf{x})$. Finally, the algorithm evaluates the normalized contrast $y_k = \bar{\eta}(\mathbf{x}_k)$ at the new point \mathbf{x}_k , and updates the dataset with \mathbf{x}_k and y_k for use in the next iteration (Lines 13 and 14). The final optimal solution is the best observation found among points of the dataset recommended by the algorithm (Line 17).

Algorithm 1 Bayesian optimization with noiseless observations

```
1: input: domain  $\mathcal{P}$  of design parameters  $\mathbf{p}$ , number of initial observations  $N$ , threshold  
   for number of BO iterations  $K$ , reparameterization map  $\phi(\cdot)$   
2: Generate  $N$  initial observations of optimization parameters  $\mathbf{x}$   
3: for  $i = 1 : N$  do ▷ Generate initial observations of the normalized contrast  
4:    $y_i \leftarrow \bar{\eta}(\mathbf{x}_i)$   
5: end for  
6:  $\mathcal{D}_0 \leftarrow \{\mathbf{x}_i, y_i\}_{i=1}^N$  ▷ Dataset of initial observations  
7:  $\{\mathbf{x}_{\min}, y_{\min}\} \leftarrow \min\{y_i, i = 1, \dots, N\}$  ▷ The best observation found so far  
8: for  $i = N + 1 : N + K$  do  
9:    $k \leftarrow i - N$   
10:  Build a GP posterior  $\hat{\eta}_k(\mathbf{x})|\mathcal{D}_{k-1}$   
11:  Formulate an acquisition function  $q(\mathbf{x}|\mathcal{D}_{k-1})$  from  $\hat{\eta}_k(\mathbf{x})|\mathcal{D}_{k-1}$   
12:   $\mathbf{x}_k \leftarrow \arg \max_{\mathbf{x}} q(\mathbf{x}|\mathcal{D}_{k-1})$  s.t.  $\phi^{-1}(\mathbf{x}) \in \mathcal{P}; \mathbf{x} \notin \mathcal{D}_{k-1}$  ▷ Maximize the acquisition  
   function  
13:   $y_k \leftarrow \bar{\eta}(\mathbf{x}_k)$  ▷ Obtain a new observation of the normalized contrast  
14:   $\mathcal{D}_k \leftarrow \mathcal{D}_{k-1} \cup \{\mathbf{x}_k, y_k\}$  ▷ Update the dataset of observations  
15:   $\{\mathbf{x}_{\min}, y_{\min}\} \leftarrow \min\{y_{\min}, y_k\}$  ▷ The best observation found so far  
16: end for  
17: return  $\{\mathbf{x}_{\min}, y_{\min}\}$  and  $\mathbf{p}_{\min} \leftarrow \phi(\mathbf{x}_{\min})$ 
```

Table 1: Carrier concentrations of InAs and layer thickness for the best 3-layer InAs structures from LCB and PI.

Parameter	LCB	PI
N_1 ($\times 10^{17}$ atoms/cm ³)	3.353	3.367
N_2 ($\times 10^{17}$ atoms/cm ³)	5.212	5.181
N_3 ($\times 10^{17}$ atoms/cm ³)	7.353	7.367
t_1 (nm)	1243	1247

Results and discussion

We present the optimization results for two nonreciprocal thermal emitters: a 3-layer InAs structure and a 6-layer 3InAs+3Weyl structure (i.e., three layers of InAs on top of three layers of Weyl semimetal). By considering these structures, we aim to investigate how a combination of InAs and Weyl semimetal can improve broadband nonreciprocity. For this purpose, we also optimize other two emitters, namely a 5-layer InAs structure and a 8-layer 5InAs+3Weyl structure, for which the optimization results are provided in the Supporting Information. The contrast between absorptivity and emissivity of the resulting optimal

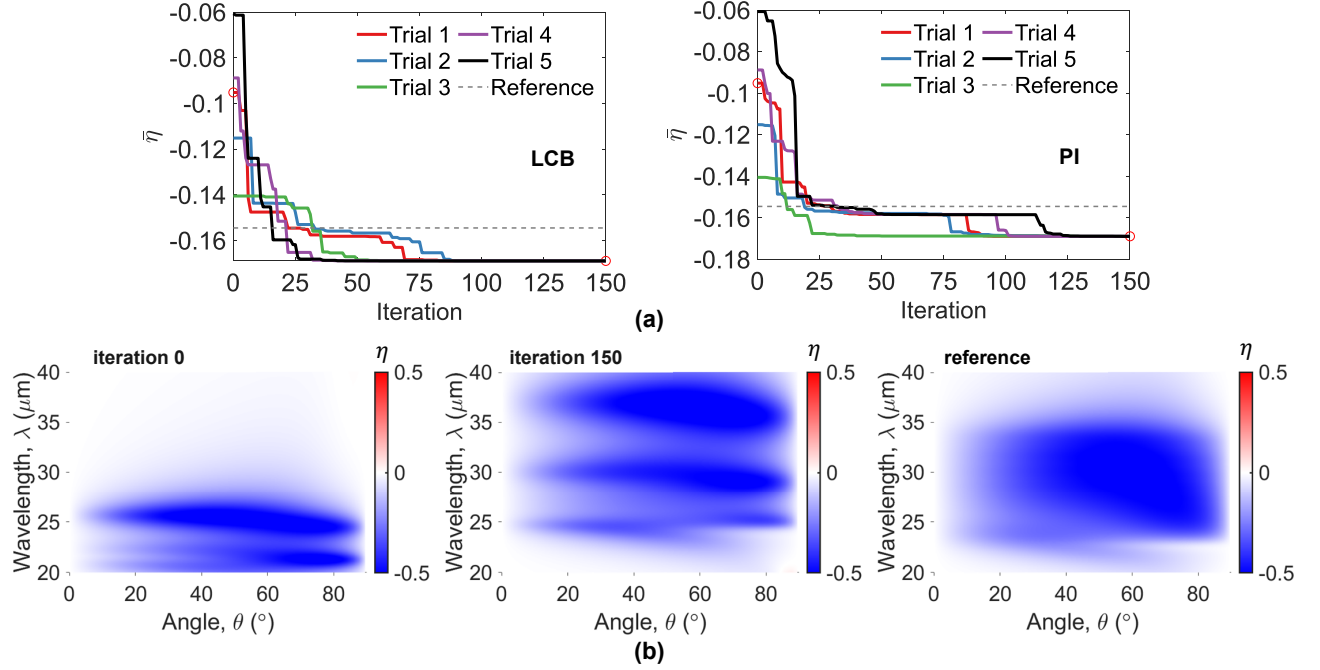


Figure 4: Optimization results for 3-layer InAs structure in comparison with the state-of-the-art 10-layer InAs structure (reference).⁹ (a) Optimization histories from LCB and PI. (b) Comparison of contrast values of the initial and final structures from the first and last iterations of the first LCB trial, and the state-of-the-art 10-layer InAs structure.

structures is compared with that of the state-of-the-art 10-layer InAs structure proposed by Du and Zhao.

Initialization

We consider wavelengths λ ranging from 5 to 40 μm , which fall within the mid-infrared region of the infrared radiation spectrum. We analyze TM waves under an applied magnetic field of $B = 1.5$ T along the $-z$ direction. The separation direction of Weyl points **2b** in all Weyl semimetal layers aligns along the $-z$ direction. Each structural reparameterization is carefully designed to ensure that the carrier concentrations of InAs and the Weyl Fermi levels across the layers conform to a polynomial of up to second order. Further details on this reparameterization scheme are provided in the Supporting Information.

There are several settings for BO and the optimizer used for maximizing the acquisition function at each BO iteration. The GP prior is determined by a zero-mean function and the

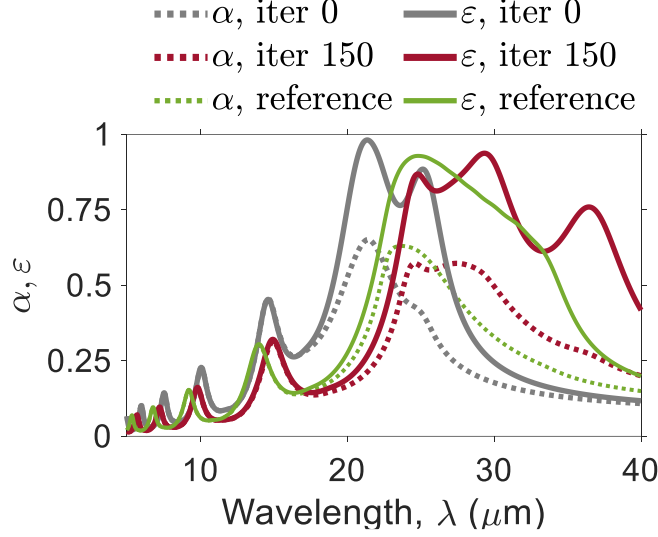


Figure 5: Absorptivity (α) and emissivity (ε) of the initial and final 3-layer InAs structures from the first and last iterations of the first LCB trial, and the state-of-the-art 10-layer InAs structure (reference).⁹

squared exponential (SE) covariance function. Design domains for the carrier concentration of InAs layers, the Fermi level of Weyl semimetal layers, and the layer thickness are $[1, 10] \times 10^{17}$ atoms/cm³, $[10^{-3}, 0.5]$ eV, and $[100, 5000]$ nm, respectively. The number of initial observations to initialize BO is $N = 5d$, where d is the number of optimization parameters \mathbf{x} . The threshold for the number of BO iterations is set at $K = 150$ for 3-layer InAs structure and at $K = 1000$ for 6-layer 3InAs+3Weyl structure. BO formulates two canonical improvement-based acquisition functions, namely the lower confidence bound (LCB) and probability of improvement (PI). Their analytical formulas are provided in the Supporting Information. To maximize each of these acquisition functions, BO uses a multi-start local optimization algorithm with 500 random starting points over the space of \mathbf{x} . The tolerance for the first-order optimality measure and the upper bound on the magnitude of any constraint functions are set at 10^{-16} . BO is implemented in MATLAB and executed on the Carya Cluster at the University of Houston.

Optimizing 3-layer InAs structure

Figure 4 show the optimization results for the 3-layer InAs structure obtained from five different BO trials of LCB and five different trials of PI, with each set of trials utilizing distinct initial datasets. Despite starting at different initial values, all five BO trials for each acquisition function converge to a unique normalized contrast value after 150 iterations, see Fig. 4(a). Figure 4(b) compares the contrast values of the 3-layer InAs structure from the first and last iterations of the first BO trial of LCB with that from the state-of-the-art 10-layer InAs structure. Although it starts from a less effective initial structure, BO provides an optimal structure with negative contrast better than that of the state-of-the-art structure, confirming its crucial role in enhancing the nonreciprocity of the 3-layer InAs structure.

Table 1 lists the optimal parameters for the best 3-layer InAs structures obtained from LCB and PI. The optimal structures from these acquisition functions are almost identical. Notably, the carrier concentrations of these optimal structures exhibit a linear increase from the top to the bottom layers. (To do: Any additional interpretation on this result?)

Figure 5 shows the absorptivity and emissivity over the considered range of incidence angles for the 3-layer InAs structures from the first and last iterations of the first BO trial using LCB, as well as those of the state-of-the-art structure. We see that BO enhances the nonreciprocity of the 3-layer InAs structure by increasing the absorptivity at wavelength values from 25 to 40 μm , which correspond to the upper region of the considered spectrum. (To do: Any additional interpretation on this result?)

Optimizing 6-layer 3InAs+3Weyl structure

Figure 6 presents the optimization results for the 6-layer 3InAs+3Weyl structure. Although different BO trials for this structure using LCB and PI do not converge to a single contrast value after 1000 iterations, they demonstrate significant improvements in the nonreciprocity. The best structures recommended by LCB and PI achieve the same negative contrast value of $\bar{\eta} = -0.244$, which is notably superior to that of the optimal 3-layer InAs structure with

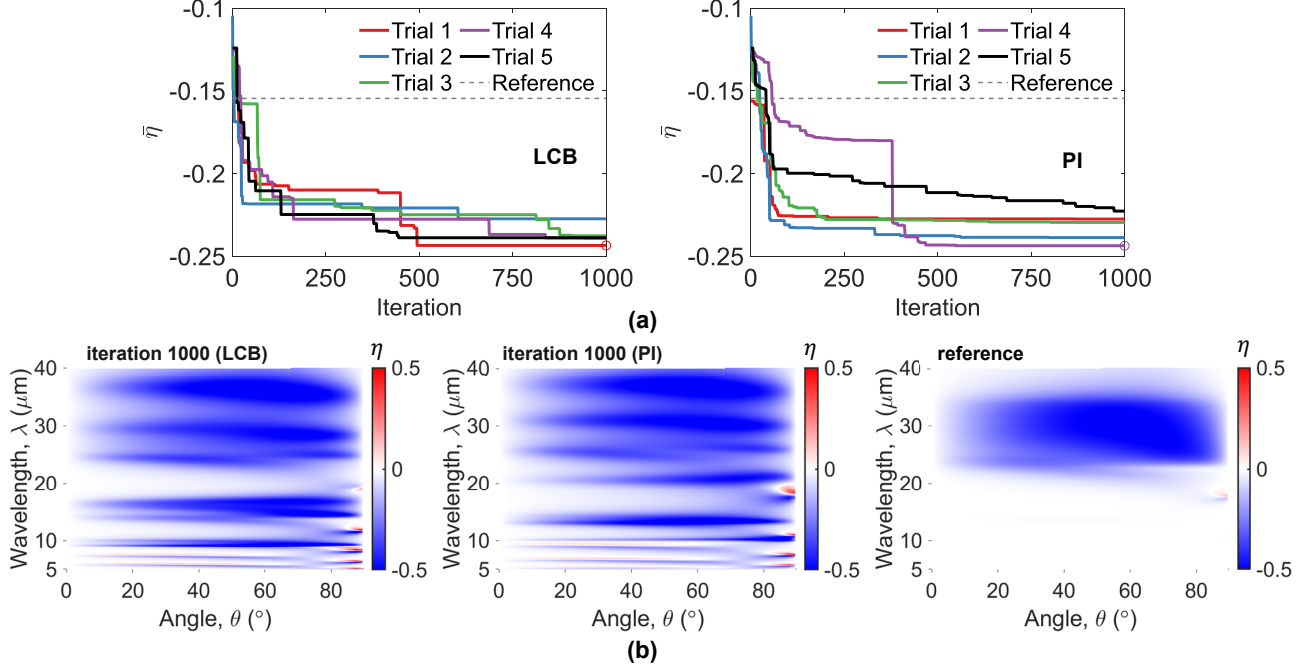


Figure 6: Optimization results for 6-layer 3InAs+3Weyl structure in comparison with the state-of-the-art 10-layer InAs structure (reference).⁹ (a) Optimization histories from LCB and PI. (b) Comparison of contrast values of the best structures from LCB and PI, and the state-of-the-art 10-layer InAs structure.

$\bar{\eta} = -0.169$ and that of the state-of-the-art 10-layer InAs structure with $\bar{\eta} = -0.154$.

As shown in Fig. 6(b) and Fig. 7, the use of three InAs layers atop three Weyl semimetal layers enhances the nonreciprocity at wavelengths in both the lower and upper regions of the considered spectrum. Specifically, the top InAs layers improve the absorptivity at wavelength values from 25 to 40 μm while the bottom Weyl semimetal layers focus on improving the absorptivity at wavelengths from 5 to 15 μm . (To do: Any additional interpretation on this result?)

Table 2 lists the optimal parameters for the best 6-layer 3InAs+3Weyl structures obtained from LCB and PI. While the two acquisition functions yield the same optimal contrast value ($\bar{\eta} = -0.244$), they provide two different sets of optimal parameters. Nevertheless, the carrier concentrations of the InAs layers of these optimal structures still increase linearly from the top to the bottom. Additionally, the thickness of the Weyl semimetal layers reaches the lower bound of its defined domain.

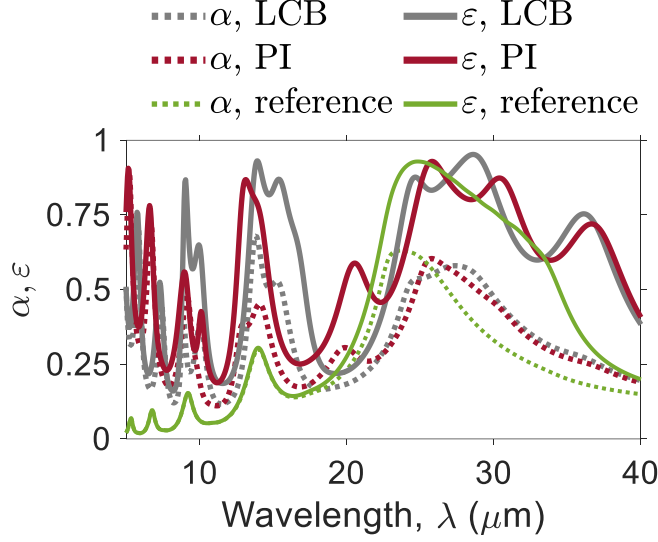


Figure 7: Absorptivity (α) and emissivity (ε) of the best 6-layer 3InAs+3Weyl structures from LCB and PI, and the state-of-the-art 10-layer InAs structure (reference).⁹

Table 2: Carrier concentrations of InAs, Fermi levels, and layer thicknesses for the best 6-layer 3InAs+3Weyl structures from LCB and PI.

Parameter	LCB	PI
N_1 ($\times 10^{17}$ atoms/cm ³)	3.416	3.308
N_2 ($\times 10^{17}$ atoms/cm ³)	5.454	4.861
N_3 ($\times 10^{17}$ atoms/cm ³)	7.416	6.777
t_1 (nm)	1203	1066
μ_1 (eV)	0.097	0.061
μ_2 (eV)	0.148	0.103
μ_2 (eV)	0.097	0.132
t_2 (nm)	100	100

Conclusion

We have presented a BO approach that can achieve optimal broadband nonreciprocal effect in the infrared range of thermal radiation using InAs and Weyl semimetal materials. Starting from a less effective structure, the proposed approach incrementally improves the broadband nonreciprocity of the structure by repeatedly constructing a probabilistic surrogate model for the normalized contrast, maximizing a cheap-to-compute acquisition function formulated from the constructed surrogate model to identify a promising new structure, and updating the surrogate model with the new structure. The optimal structure is the best structure

among those recommended by the optimization algorithm upon its termination. Optimization results indicate that our approach can propose an optimal structure of only three InAs layers that outperforms the current state-of-the-art 10-layer InAs structure.⁹ Additionally, the broadband nonreciprocal effect considerably increases when using InAs layers atop Weyl semimetal layers, thanks to the enhanced absorptivity at wavelengths in both the upper and lower regions of the considered spectrum. In an ongoing study, we conduct experiments to validate the performance of the optimized structures. We then combine the experimental and numerical observations within the framework of multi-fidelity BO¹⁰ to further enhance our design approach. (To do: Revise the conclusion and add the potential significance of the findings?)

Acknowledgement

Associated content

Data availability statement The data underlying this study are not publicly available as they form part of an ongoing study. The code for Bayesian optimization is available from the first author upon reasonable request.

Supporting information The mathematical foundation of Gaussian process, the analytical solutions of LCB and PI acquisition functions, the quadrature method for computing the contrast between absorptivity and emissivity at a particular value of design parameters, the details of the reparameterization scheme, and additional results.

References

- (1) Snoek, J.; Larochelle, H.; Adams, R. P. Practical Bayesian optimization of machine learning algorithms. *Advances in Neural Information Processing Systems*. 2012; pp

2951–2959.

- (2) Garnett, R. *Bayesian optimization*; Cambridge University Press, 2023.
- (3) Rasmussen, C. E.; Williams, C. K. I. *Gaussian processes for machine learning*; The MIT Press: Massachusetts, USA, 2006.
- (4) Jones, D. R.; Schonlau, M.; Welch, W. J. Efficient global optimization of expensive black-box functions. *Journal of Global Optimization* **1998**, *13*, 455–492.
- (5) Jones, D. R. A taxonomy of global optimization methods based on response surfaces. *Journal of Global Optimization* **2001**, *21*, 345–383.
- (6) Villemonteix, J.; Vazquez, E.; Walter, E. An informational approach to the global optimization of expensive-to-evaluate functions. *Journal of Global Optimization* **2009**, *44*, 509–534.
- (7) Hennig, P.; Schuler, C. J. Entropy search for information-efficient global optimization. *Journal of Machine Learning Research* **2012**, *13*, 1809–1837.
- (8) Wang, Z.; Jegelka, S. Max-value entropy search for efficient Bayesian optimization. Proceedings of the 34th International Conference on Machine Learning. 2017; pp 3627–3635.
- (9) Du, C.; Zhao, B. Controlling the ENZ profile for broadband nonreciprocal thermal emitters with high contrast between emissivity and absorptivity. The Proceedings of the 10th International Symposium on Radiative Transfer (RAD-23). 2023; pp 111–118.
- (10) Do, B.; Zhang, R. Multi-fidelity Bayesian optimization in engineering design. *arXiv preprint arXiv:2311.13050* **2023**,